ADVANCED MATERIALS

www.advmat.de

Linear Dichroism Conversion in Quasi-1D Perovskite Chalcogenide

Jiangbin Wu, Xin Cong, Shanyuan Niu, Fanxin Liu, Huan Zhao, Zhonghao Du, Jayakanth Ravichandran, Ping-Heng Tan,* and Han Wang**

Anisotropic photonic materials with linear dichroism are crucial components in many sensing, imaging, and communication applications. Such materials play an important role as polarizers, filters, and waveplates in photonic devices and circuits. Conventional crystalline materials with optical anisotropy typically show unidirectional linear dichroism over a broad wavelength range. The linear dichroism conversion phenomenon has not been observed in crystalline materials. The investigation of the unique linear dichroism conversion phenomenon in quasi-1D hexagonal perovskite chalcogenide $BaTiS_3$ is reported. This material shows a record level of optical anisotropy within the visible wavelength range. In contrast to conventional anisotropic optical materials, the linear dichroism polarity in $BaTiS_3$ makes an orthogonal change at an optical wavelength corresponding to the photon energy of 1.78 eV. First-principles calculations reveal that this anomalous linear dichroism conversion behavior originates from the different selection rules of the parallel energy bands in the $BaTiS_3$ material. Wavelength-dependent polarized Raman spectroscopy further confirms this phenomenon. Such a material, with linear dichroism conversion properties, could facilitate the sensing and control of the energy and polarization of light, and lead to novel photonic devices such as polarization-wavelength selective detectors and lasers for multispectral imaging, sensing, and optical communication applications.

Linear dichroism is the difference between the absorption of light polarized along the perpendicular and parallel directions with respect to a specific orientation axis of a natural or artificial crystal.[1] Strong linear dichroism can be obtained by designing the micro/nanostructures in metamaterials, which can be used in optical components including polarizers and wave plates.[2–6] In naturally occurring crystals, the linear dichroism typically arises from the reduced symmetry in the crystal lattice that depends on the specific crystal structure and the elemental composition.[7–14] Besides improving the performance of traditional optical components, these anisotropic crystals can enable polarization-sensitive photonic devices[15–20] important for many emerging sensing and communication applications.

Materials with strong optical anisotropy usually have a reduced level of crystal symmetry which often exists among low-dimensional crystals, such as 2D[10] and 1D materials,[21] as well as in bulk materials.[22] Layered black phosphorus

---

Dr. J. Wu, H. Zhao, Z. Du, Prof. H. Wang
Ming Hsieh Department of Electrical and Computer Engineering
University of Southern California
Los Angeles, CA 90089, USA
E-mail: han.wang.4@usc.edu

X. Cong, Prof. P.-H. Tan
State Key Laboratory of Superlattices and Microstructures
Institute of Semiconductors
Chinese Academy of Sciences
Beijing 100083, P. R. China
E-mail: phtan@semi.ac.cn

X. Cong, Prof. P.-H. Tan
College of Materials Science and Opto-Electronic Technology &
CAS Center of Excellence in Topological Quantum Computation
University of Chinese Academy of Science
Beijing 100049, P. R. China

S. Niu, Prof. J. Ravichandran, Prof. H. Wang
Mork Family Department of Chemical Engineering and Materials Science
University of Southern California
Los Angeles, CA 90089, USA
E-mail: jayakanr@usc.edu

Prof. F. Liu
Collaborative Innovation Center for Information Technology in Biological and Medical Physics
and College of Science
Zhejiang University of Technology
Hangzhou 310023, P. R. China

The ORCID identification number(s) for the author(s) of this article can be found under https://doi.org/10.1002/adma.201902118.

DOI: 10.1002/adma.201902118

(BP) with reduced in-plane crystal symmetry has attracted remarkable attention due to the strong anisotropy of its vibrational,[23] optical,[9,24] and electrical properties.[10] Other 2D and 1D materials, such as ReX_2 (X = S and Se),[12,13] AX (A = Ge, Sn, and Tl; X = S, Se, and As)[25–30] and carbon nanotubes,[31] have also demonstrated linear dichroism. However, in those materials, the linear dichroism polarity is uniform within a very broadband wavelength range, i.e., the absorption of light polarized along one particular direction is always stronger than that along other directions.[16,25,26] Recently, members of the ternary perovskite chalcogenides family[32,33] including $BaTiS_3$[34] and $Sr_{1-x}TiS_3$[35] were demonstrated to possess pronounced anisotropic optical responses in the mid-wave infrared (MWIR) and long-wave infrared (LWIR) spectral ranges. In those materials, the TiS_6 octahedra form the parallel quasi-1D lattice chains. The large birefringence and linear dichroism in the MWIR and LWIR wavelength ranges result from the significant anisotropy of structure and chemical composition between the intra- and inter-chain directions.

In this work, we reveal a unique linear dichroism conversion phenomenon in the quasi-1D $BaTiS_3$ material. Observed using reflectance anisotropy spectroscopy, the ultrahigh level of linear dichroism in $BaTiS_3$ in the visible range exceeds that in any other crystalline materials, and an anomalous linear dichroism conversion occurs at the 1.78 eV photon energy. Density functional theory (DFT) calculations show that the linear dichroism conversion originates from the polarization-resolved localized joint density of states of the material due to its parallel band structure in this optical transition energy range. Furthermore, wavelength dependent polarized Raman spectroscopy also evidenced this linear dichroism phenomenon. The resulting unique wavelength and crystal-orientation dependent optical properties of $BaTiS_3$ can open door to new opportunities for enabling wavelength tunable and polarization sensitive photonic devices desired for emerging applications in optical communication, imaging, and sensing.

Millimeter-size single-crystal $BaTiS_3$ was synthesized using an iodine based vapor transport method.[34] The $BaTiS_3$ crystal lattice form a hexagonal structure as illustrated in **Figure 1**a,b. This quasi-1D crystal consists of parallel chains of TiS_6 octahedra sharing common faces along the *c*-axis, about which the material has sixfold rotation symmetry.[32–35] The Ba ions are enclosed within the hexagonal TiS_6 structure. The interaction within the TiS_6 cell is much stronger than that among the TiS_6 cells. This resembles 2D layered materials that have strong in-plane covalent bonding but only weak van der Waals interlayer interactions. Thus, bulk $BaTiS_3$ can be exfoliated into thin flakes with thickness below tens of nanometers, as shown in the optical micrograph in Figure 1c. The sample thickness is measured by the atomic force microscopy (AFM) (Figure S1, Supporting Information). The elemental composition of $BaTiS_3$ is confirmed by the energy-dispersive X-ray spectroscopy (EDS) mapping (Figure 1d). The quasi-1D chains of $BaTiS_3$ and their hexagonal arrangements are revealed by the high-resolution transmission electron microscopy (HR-TEM) measurements imaged along the *c*-axis (Figure 1f) and *a*-axis (Figure 1g) of

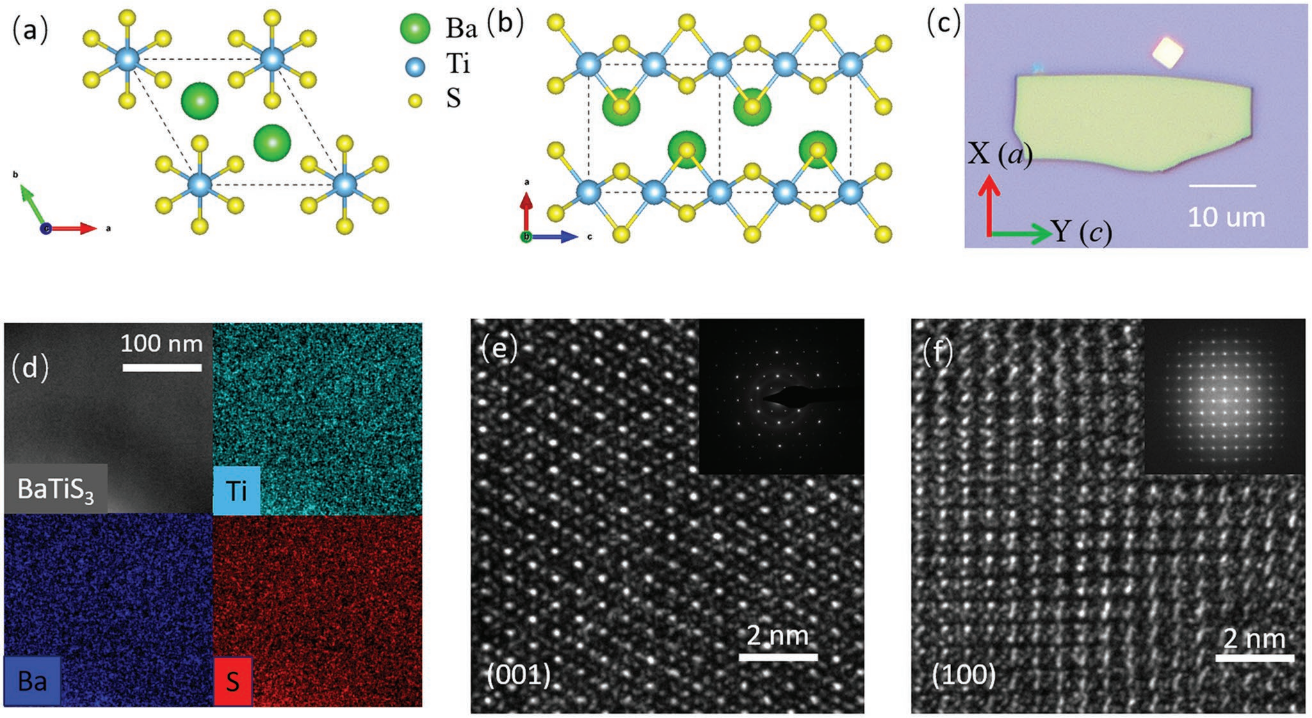

Figure 1. Schematic lattice structure of the $BaTiS_3$ lattice viewed along a) the *c*-axis and b) the *a*-axis of the crystal. The *c*-axis view of the crystal in (a) has hexagonal symmetry and the *a*-axis view of the crystal in (b) illustrates the TiS_6 chains along the *c*-axis. c) Optical micrograph of $BaTiS_3$ sample mechanically cleaved along *a*–*c* plane. d) EDS image of the elemental composition in the $BaTiS_3$ lattice showing the titanium (cyan), barium (blue), and sulfur (red). The scale bar is 100 nm. Atomic resolution TEM imaged along e) the *c*-axis and f) *a*-axis of the $BaTiS_3$ crystal. The corresponding electron diffraction patterns are shown as the insets.

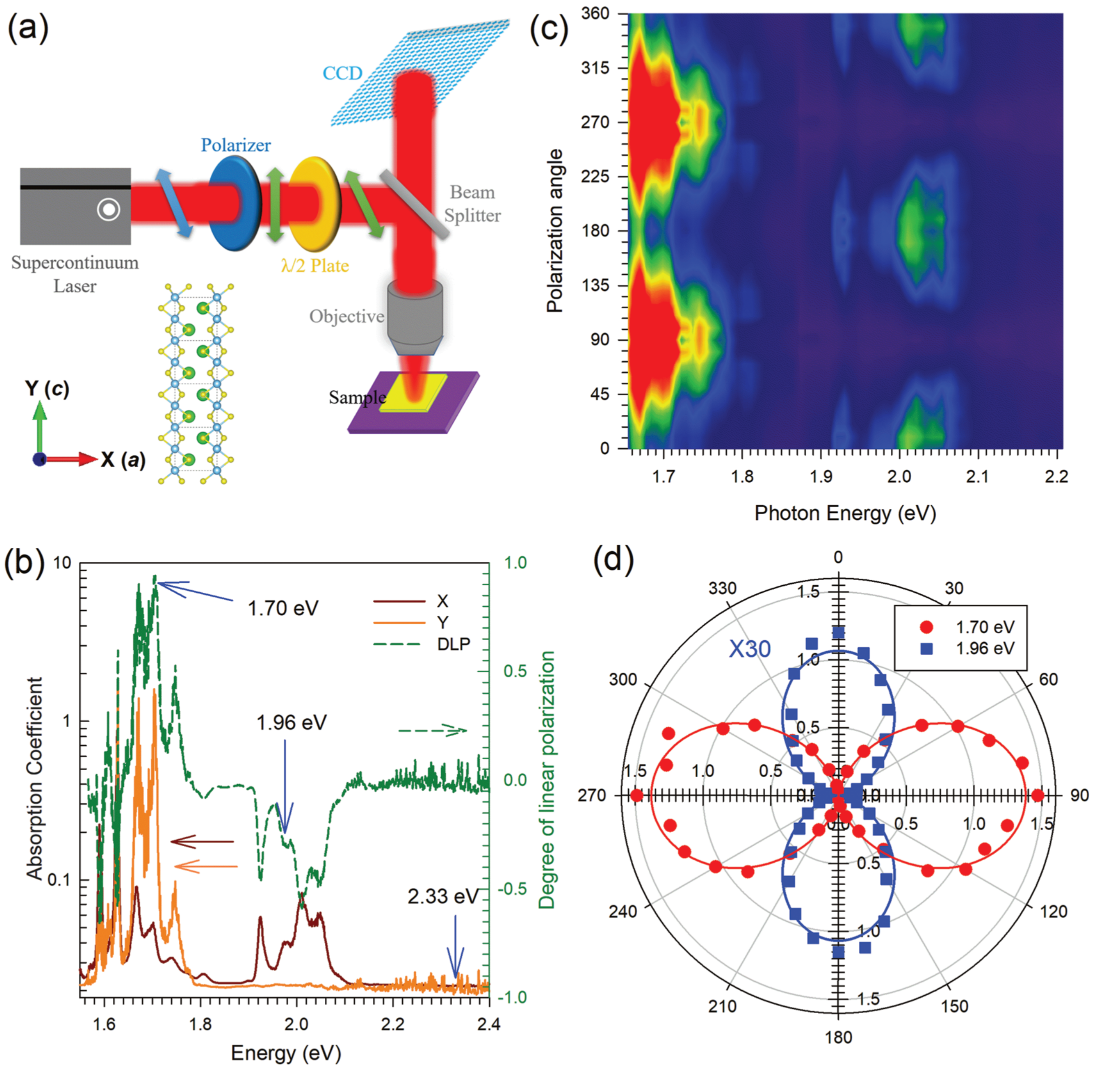

Figure 2. a) Schematic illustration of the characterization system for measuring the polarization-resolved optical absorption. b) Absorption coefficients in response to the X- and Y-polarized beam and the degree of linear polarization (DLP) in the visible range. c) The absorption spectra as a function of both the excitation photon energy and the polarization direction. The color pattern in the spectra indicates the anisotropy in the reflection coefficients. d) Polar plots of the absorption coefficients with changes in the incident beam polarization angle at two different excitation photon energies of 1.70 and 1.96 eV, respectively. The red dots and blue squares show the experimental data. The red and blue lines are the fitted curves.

the crystal. Corresponding electron diffraction images are also presented in Figure 1e,f, which show the hexagonal and square reciprocal space along the *c*-axis and *a*-axis, respectively.

To experimentally characterize the linear dichroism of $BaTiS_3$, a supercontinuum laser source (NTK SuperK EXTREME OCT) is employed, whose laser beam is polarized by a broadband polarizer (see the Experimental Section). The polarization angle of the incident laser light is tuned by a broadband half-wave plate, as shown in **Figure 2**a. Here, we define the X axis of the incident light as being parallel to the *a*-axis of the $BaTiS_3$ lattice while the *Y* axis of the incident laser is along the *c*-axis of the crystal. The reflected light is detected by a charge-coupled device (CCD) camera. All the reflectance measurements are normalized with respect to a reference spectrum measured from a silver mirror. The measured reflectance with the incident laser polarization along both the *X*- and *Y*-directions is presented in Figure S2 in the Supporting Information. Based on the Kramers–Kronig transform[36] of the reflectance data, we can calculate the absorption coefficient of the material as a function of the optical frequency (see the Supporting Information for details).

Figure 2b presents the measured absorption spectra with the incident laser polarization along both the *X*- and *Y*-directions (A_x and A_y) in the photon energy range from 1.5 to 2.7 eV. Among other existing materials showing linear dichroism, it is commonly observed that the absorption of light polarized along one crystal direction is always stronger than that along other crystal directions over a broad wavelength range. However, the linear dichroism polarity in $BaTiS_3$ shows a significant dependence on wavelength. As shown in Figure 2b, A_y has much stronger intensity than A_x in the photon energy range from 1.6 to 1.78 eV. As the photon energy increases above 1.78 eV, however, the dominant axis of the linear dichroism changes to a different direction that is almost orthogonal to that below 1.78 eV. When the photon energy reaches above 2.15 eV, A_x becomes close to A_y and the linear dichroism is much weaker. Hence, A_x and A_y show a clear crossover at 1.78 eV, i.e., the linear dichroism conversion at 1.78 eV. Here we define the degree of linear polarization (DLP) as $(A_y - A_x)/(A_x + A_y)$, which has values within the range from −1 to 1. A DLP value between −1 and 0 means $A_y < A_x$, and a DLP value between 0 and 1 will indicate $A_y > A_x$. Moreover, the larger magnitude of DLP indicates stronger linear dichroism. When the photon energy is below 1.78 eV, the DLP is observed to be less than 0, and it becomes greater than 0 for photon energies above 1.78 eV. At the photon energy range between 1.65 and 1.71 eV, the magnitude of the DLP reaches above 0.9, indicating the ultrahigh level of linear dichroism in $BaTiS_3$ within this wavelength range. This DLP is much higher than that in other naturally existing materials with strong linear optical dichroism including black phosphorus[9] and ReS_2.[37] It is also close to the record value achieved in the artificial plasmonic metasurfaces.[2]

Polarization-resolved absorption spectra are observed by varying the polarization angle (θ), which is defined as the angle between the polarization of the incident beam and the *a*-axis of the crystal, from 0° to 360°, as shown in Figure 2c. At the vicinity of 1.7 eV photon energy, the maximum reflectance is observed at the angle of 90° and 270°, and for photon energy around 2.0 eV, the maximum reflectance is observed at the angle of 0° and 180°. Figure 2d shows the polar plots of the reflectance at the photon energies of 1.70 and 1.96 eV, respectively. This agrees with the results shown in Figure 2b,c. As the polarization angle θ is varied, the absorption (A) shows periodic changes, which can be fitted by: $A = (A_{\max} - A_{\min})\cos 2(\theta - \theta_0) + A_{\min}$, where θ_0 denotes the reference polarization angle at which the absorption coefficient reaches the maximum. Thus, at 1.70 eV excitation energy, the reflectance reaches the maximum along the *a*-axis of the $BaTiS_3$ crystal, while at 1.96 eV excitation energy, the maximum reflectance is reached along the *c*-axis of the lattice. The results in Figure 2c hence reveals the linear dichroism conversion in the material.

To explore the origin of the linear dichroism conversion, the calculation of the polarization-resolved absorption spectra of $BaTiS_3$ is performed using DFT (see the Experimental Section), as shown in **Figure 3**a. One prominent peak is observed along the *a*-axis at 2.0 eV excitation photon energy. On the other hand, there are three narrow peaks at 1.15, 1.6, and 2.33 eV along the *c*-axis, resulting in a valley at 1.9 eV. Hence, the calculated polarization-resolved absorption spectra predict a linear dichroism conversion from 1.5 to 2.3 eV and the crossover occurs at 1.8 eV. The calculation results agree well with the experimental data. When the photon energy is larger than 2.3 eV, the theoretical results indicate that the linear dichroism becomes weak, which also agrees with the experimental results in Figure 2b. The calculated polarization-resolved reflection spectra are also presented in Figure S3 in the Supporting Information, showing good agreement with experimentally obtained reflection spectra in Figure S2 in the Supporting Information. To further understand the origin of the peaks in the absorption and reflection spectra, the band structure and density of states (DOS) in $BaTiS_3$ are calculated as presented in Figure 3b. Optical transition matrix element (dipole-transition selection rule) is also considered in the calculation. The optically-allowed transitions between a series of parallel bands corresponding to the narrow reflection peaks are indicated in Figure 3b.

Along the *a*-axis, the peak at 2.0 eV energy is assigned to the optical transitions between the p_z orbital of the sulphur atom and the d_{yz} and d_{xz} orbitals of the titanium atom. Indeed, according to calculation of dipole-transition selection rule, this transition is *a*(*b*)-axis allowed, but not *c*-axis allowed, which confirms our assignation. Along the *c*-axis, the peak at 1.15 eV energy is due to the optical transition from the p_z orbital in the sulphur atom to the d_{z^2} orbital in the titanium atom. The transitions between the d_{yz} and d_{xz} orbital in the titanium atom and the p_x and p_y orbitals in the sulphur atom lead to the peak at 1.6 eV. Moreover, the peak at 2.3 eV originates from the transition between the d_{xy} and $d_{x^2-y^2}$ orbitals in the Ti atom and the p_z orbital in the S atom. We confirm that those transitions are *c*-axis allowed, but not *a*(*b*)-axis allowed. The orbitals corresponding to the relevant energy bands (the high symmetry path of first Brillouin zone is shown in Figure S4 in the Supporting Information) are labeled in Figure 3b. Figure 3c–g shows the partial charge densities for the states in Figure 3b. It is worth noting that the highlighted conduction and valence bands in Figure 3b are almost parallel to each other, which resembles the band structure features in twisted bilayer graphene.[38–40] These parallel bands would lead to the singularities injoint density of states, i.e., absorption peaks, at the specific photon energies. In the twisted bilayer graphene, the localized joint density of states leads to absorption wavelength (photon energy) that is highly dependent on the twisting angles between the two graphene layers. Here, the wavelength dependence of the linear dichroism polarity (linear dichroism conversion) arises in $BaTiS_3$ due to the absorption peaks along the two principal crystal directions being strongly localized at different energies.

The Raman spectroscopy can reveal polarization-resolved phonon characteristics in many nanomaterials. Indeed, the Raman tensor of low-symmetry crystal always shows a high level of anisotropy.[41–43] However, the Raman scattering process typically involves both electron–phonon (Raman tensor) and electron–photon interactions (dipole-transition selection rule).[42] According to the second-order perturbation theory, the polarization-resolved Raman intensity $\mathrm{I}(\theta) \propto |M_{eR}^{i}(\theta) \bullet M_{ph}(\theta) \bullet M_{eR}^{s}(\theta)|^2$, where $M_{eR}^{i}(\theta)$ and $M_{eR}^{s}(\theta)$ are the incident and scattered optical transition matrix elements, respectively, and $M_{ph}(\theta)$ is the matrix element value related to the electron–phonon coupling.[44] As illustrated in **Figure 4**a, the Raman spectra of $BaTiS_3$ are measured at the excitation energy of 1.71, 1.96, and 2.33 eV lasers with the incident light polarization along the *a*-axis. There are two prominent peaks at 186 and 380 wavenumbers. The normal mode displacements of these two phonon modes are calculated based on density functional perturbation theory (DFPT) and shown in Figure 4b. Because the $BaTiS_3$ has a D_{6h} symmetry, according the vibrational displacement, we classified these two phonon modes as A_{1g}, and denoted them as A_{1g}^1 and A_{1g}^2 based on their frequencies, respectively.

Since the A_{1g}^1 mode disappears at 1.71 and 1.96 eV excitations, here we focus on discussing the A_{1g}^2 mode. Figure 4c,d shows the polarization-resolved Raman spectra and intensity of the A_{1g}^2 mode under the three-excitation wavelengths at 1.71,

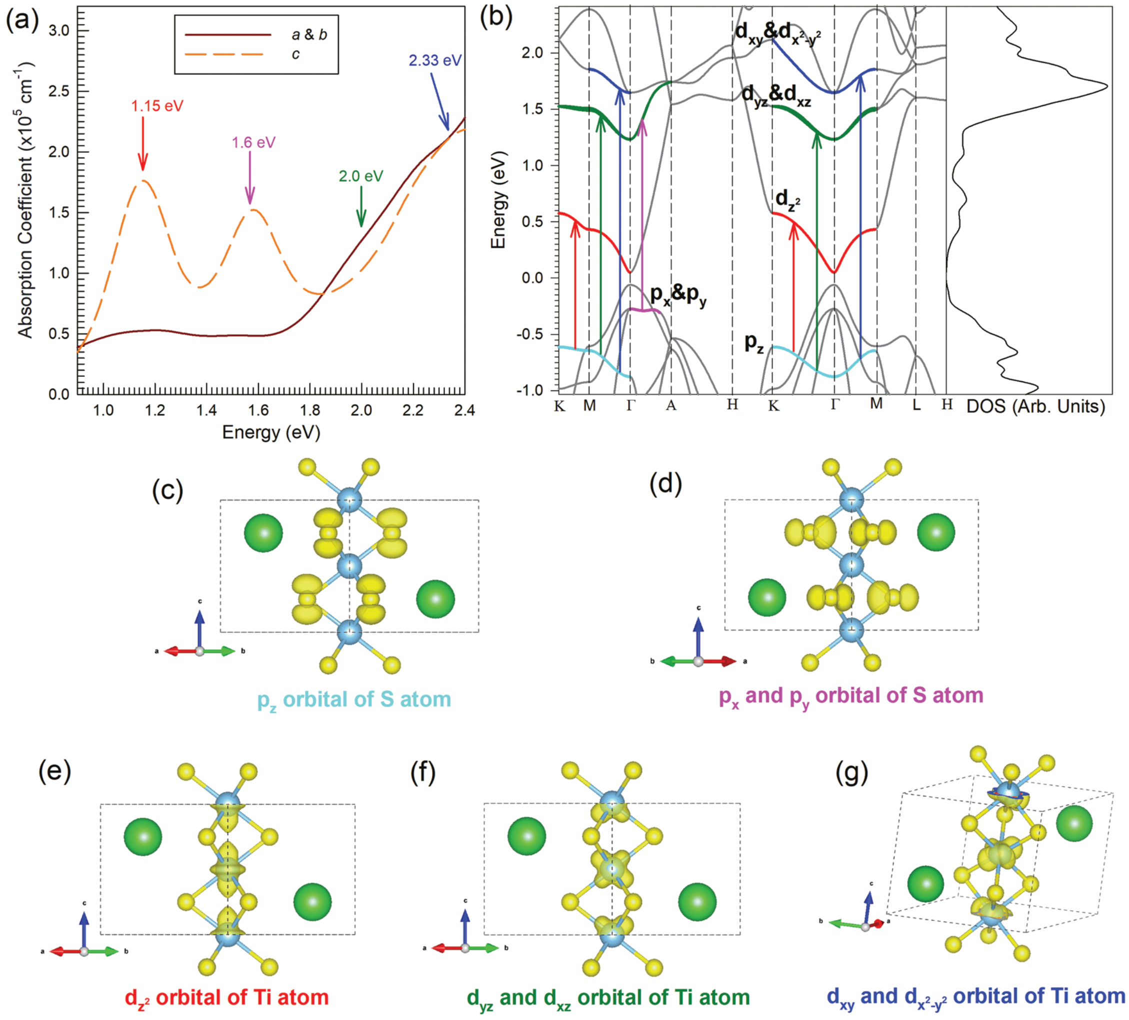

Figure 3. a) The absorption spectra calculated using DFT for excitation light polarized along *c*-axis and *a*(*b*)-axis. b) The theoretically calculated band structure and density of states (DOS). The orbitals of the corresponding bands are highlighted and marked. The calculated partial charge densities of the orbitals are shown in c) p$_z$ in S atom, d) p$_x$ and p$_y$ in S atom, e) d$_z$^{2} in Ti atom, f) d$_{yz}$ and d$_{xz}$ in Ti atom, and g) d$_{xy}$ and d$_{x}^{2}_{-y}$^{2} in Ti atom.

1.96, and 2.33 eV. The principal polarization orientation (the orientation of the strongest intensity) of the Raman spectra between 1.96 and 2.33 eV are almost perpendicular (≈85°), and those of 1.71 and 2.33 eV are parallel to each other. To understand the underlying mechanism, we consider both electron–photon and electron-phonon couplings. The Raman tensor of the A_{1g} mode is[45]

$$A_{1g} = \begin{bmatrix} a & 0 & 0 \\ 0 & a & 0 \\ 0 & 0 & b \end{bmatrix}$$

For the 2.33 eV excitation where there is almost no linear dichroism in BaTiS$_3$, as shown by both experiment and theory in Figures 2b and 3a, the anisotropy in $M_{eR}^{i}(\theta)$ and $M_{eR}^{s}(\theta)$ can be neglected. Thus, $I(\theta) \propto |M_{ph}(\theta)|^2 \propto |a\sin\ \theta|^2 + |b\cos\ \theta|^2$ according to Raman tensor.[44] Therefore, the principal polarization orientation under the excitation of 2.33 eV is determined by the ratio of a^2/b^2. By fitting the experimental data, we can extract the value of a^2/b^2 to be 1.62. This indicates the dependence of the phonon mode intensity ($|M_{ph}(\theta)|^2 \propto 0.62|\sin\ \theta|^2 + 1$) on the polarization direction and the strong electron–phonon interaction occurs along the crystal direction that is almost parallel to the *c*-axis, as shown in Figure 4d. At other wavelengths (for example, 2.71 eV, as shown in Figure S5 in the Supporting Information) where the linear dichroism is also week (as shown in Figures S2 and S3 in the Supporting Information), the linear dichroism also can be neglected, the principal polarization orientation of the A_{1g}^2 mode should be the same as that under the excitation of 2.33 eV and with the similar a^2/b^2 (as shown in Figure S4 in the Supporting Information). However, due to the presence of strong linear dichroism at 1.96 eV excitation energy, the principal polarization orientation of the A_{1g}^2 mode becomes almost parallel to that of the absorption, i.e., almost perpendicular (≈85°) to that of the A_{1g}^2 mode under the excitation of 2.33 eV photon energy. It indicates that the linear dichroism plays a more dominant role at this excitation wavelength. As a result, the principal polarization orientation

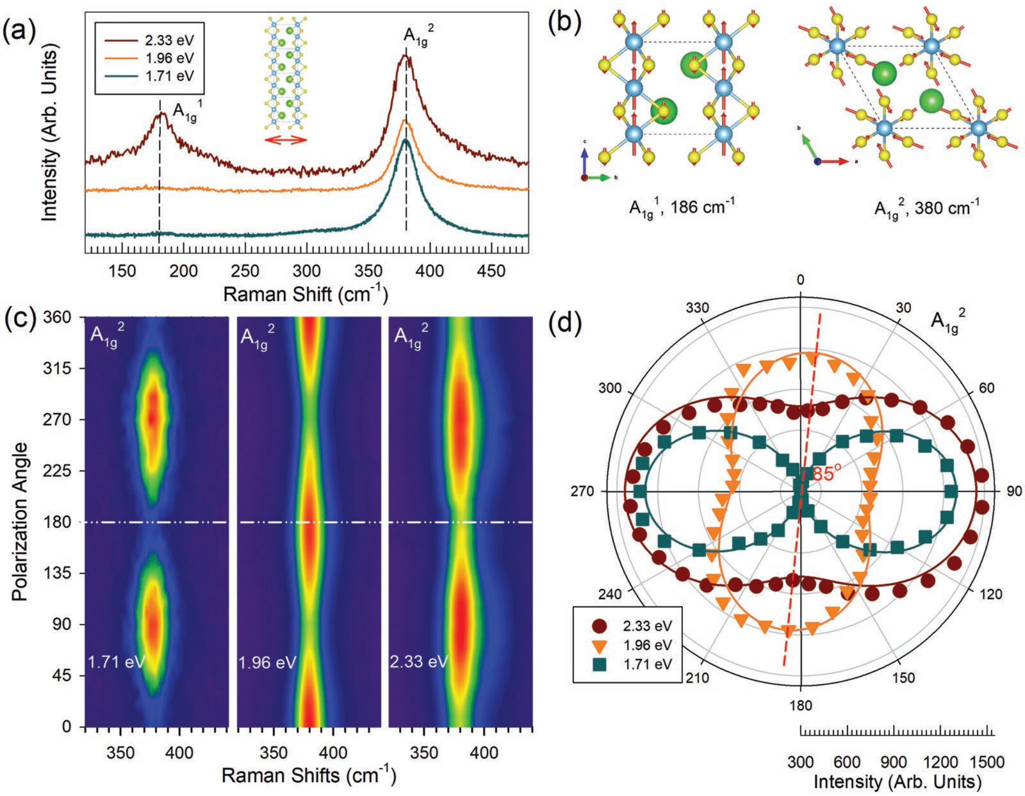

Figure 4. a) The measured Raman spectra of $BaTiS_3$ obtained with 2.33, 1.96, and 1.71 eV incident excitation energies. The incident laser is polarized along the *a*-axis of the $BaTiS_3$ crystal. b) Displacement of the corresponding phonon modes in (a) calculated by DFPT. c) Anisotropic Raman spectra in the region of A_{1g}^{2} mode plotted versus the Raman shift and different polarization directions for the three excitation conditions at 1.71, 1.96, and 2.33 eV, respectively. d) Polar plots of the Raman spectra intensity of the A_{1g}^{2} mode versus the polarization angle at the 2.33, 1.96, and 1.71 eV excitations. The brown dots, orange triangles, and cyan squares are the experimental data. The brown, orange, and cyan lines are the fitted curves.

of the A_{1g}^{2} mode observed in Raman spectroscopy is dominated by the absorption instead of the electron–phonon interaction, which further confirms the strong linear dichroism of the $BaTiS_3$ under the excitation of 1.96 eV. Under the 1.71 eV excitation energy where it has the orthogonal linear dichroism compared with 1.96 eV excitation, the principal polarization orientation of the A_{1g}^{2} mode in the Raman spectrum is parallel to that with 2.33 eV excitation and shows even higher level of anisotropy. As shown in Figure 4c,d, the ratio between the maximum and minimum of θ-dependent Raman intensities: $I(\theta)_{\max}/I(\theta)_{\min}$ is 1.62 under the excitation of 2.33 eV, and $I(\theta)_{\max}/I(\theta)_{\min}$ is 3.44 for 1.71 eV excitation. Since the polarities of both the absorption and the electron-phonon-interaction align with each other (along the *c*-axis) at 1.71 eV excitation, the level of anisotropy in the Raman intensities becomes significantly enhanced compared to that with the 2.33 eV excitation. Therefore, the wavelength dependent polarities of the Raman intensities further confirm the strong linear dichroism and linear dichroism conversion properties in the $BaTiS_3$ crystal.

In summary, the strong and anomalous linear dichroism in the *a*–*c* plane of quasi-1D $BaTiS_3$ is observed through the reflectance anisotropy spectroscopy. The DLP in the material reaches a record peak value of 0.9 within the visible wavelength range. The linear dichroism reverses its polarity at the 1.78 eV excitation energy due to the singularities in joint density of states along both the *a*- and *c*- directions of the crystal resulting from the parallel band structure in $BaTiS_3$. The Raman spectroscopy measurements under the 1.71, 1.96, and 2.33 eV excitations further confirm the strong linear dichroism and linear dichroism conversion properties in the material. The unique linear dichroism conversion property found in $BaTiS_3$ ultrathin flakes can lead to novel photonic detection device, which can provide dynamically tunable responses with respect to both the wavelength and the polarization of the incident light, with broad applications in optical sensing, communications, multispectral imaging.

Experimental Section

Scanning Electron Microscope (SEM), TEM, and EDS Characterization: JEOL JSM 7001 system was used to obtain the SEM and TEM images at an accelerating voltage of 15 kV. The focused ion beam (FIB) was employed to obtain the cross-sectional samples in the direction parallel and perpendicular to the *c*-axis of the $BaTiS_3$ crystal. During the EDS imaging, magnification levels ranging from ×500 to ×15000 were employed.

DFT Calculations: DFT code Vienna ab initio simulation package (VASP)[46] was used to carry out the structural relaxation calculation.[47,48] The generalized gradient approximation (GGA) was also employed to calculate the exchange correlation potential. The GGA + U method[49] was used to give the electronic band structures, electronic charge density and the light-matter interaction properties. U is the Coulomb parameter. The first Brillouin zone of the $BaTiS_3$ unit cell was mapped using a 16 × 16 × 16 k-space mesh. The atoms within the unit cell were fully relaxed until the force per atom force was below the 0.0001 eV $Å^{-1}$ limit with a cutoff energy of 400 eV. The frequencies and vibration modes of the phonons were calculated using the DFPT method[50] realized in the VASP package.

Raman Spectroscopy: The back-scattering Raman spectra were obtained using a Jobin–Yvon HR evolution system, integrated with a ×100 objective lens and a numerical aperture of 0.90, a CCD camera cooled by liquid nitrogen, and a few gratings. The 2.33 eV excitation light was provided by a solid laser, the 1.96 eV incident light was from a He–Ne laser and the 1.71 eV light was provided by a Ti:Saphire laser. The spectral resolution of the measurement system was 0.49 cm^{-1} at 2.33 eV per pixel of the CCD camera. The power of the incident laser was kept at ≈0.5 mW.

Supporting Information

Supporting Information is available from the Wiley Online Library or from the author.

Acknowledgements

H.W., J.W., and Z.D. acknowledge the support from the Army Research Office (Grant No. W911NF-18-1-0268), the Air Force Office of Scientific Research FATE MURI program (Grant No. FA9550-15-1-0514), and the National Science Foundation (Grant No. EFMA-1542815). J.R. and S.N. acknowledge the support from the Air Force Office of Scientific Research (Grant No. FA9550-16-1-0335) and Army Research Office (Grant No. W911NF-19-1-0137). S.N. acknowledges Link Foundation Energy Fellowship. P.-H.T. acknowledges support from the National Key Research and Development Program of China (Grant No. 2016YFA0301204) and the National Natural Science Foundation of China (Grant Nos. 11874350, 11604326, 11474277, and 11434010).

Conflict of Interest

The authors declare no conflict of interest.

Keywords

linear dichroism conversion, optoelectronics, perovskite chalcogenides

Received: April 3, 2019
Revised: June 6, 2019
Published online: June 25, 2019

---

[1] A. Rodger, B. Nordén, B. Nordén, *Circular Dichroism and Linear Dichroism*, Vol. *1*, Oxford University Press, Oxford, UK **1997**.
[2] Y. Yang, W. Wang, P. Moitra, I. I. Kravchenko, D. P. Briggs, J. Valentine, *Nano Lett.* **2014**, *14*, 1394.
[3] D. Lin, P. Fan, E. Hasman, M. L. Brongersma, *Science* **2014**, *345*, 298.
[4] M. Khorasaninejad, W. T. Chen, R. C. Devlin, J. Oh, A. Y. Zhu, F. Capasso, *Science* **2016**, *352*, 1190.
[5] H.-T. Chen, A. J. Taylor, N. Yu, *Rep. Prog. Phy.* **2016**, *79*, 076401.
[6] A. E. Minovich, A. E. Miroshnichenko, A. Y. Bykov, T. V. Murzina, D. N. Neshev, Y. S. Kivshar, *Laser Photonics Rev.* **2015**, *9*, 195.
[7] J. Qiao, X. Kong, Z.-X. Hu, F. Yang, W. Ji, *Nat. Commun.* **2014**, *5*, 4475.
[8] X. Wang, A. M. Jones, K. L. Seyler, V. Tran, Y. Jia, H. Zhao, H. Wang, L. Yang, X. Xu, F. Xia, *Nat. Nanotechnol.* **2015**, *10*, 517.
[9] F. Xia, H. Wang, Y. Jia, *Nat. Commun.* **2014**, *5*, 4458.
[10] L. Li, Y. Yu, G. J. Ye, Q. Ge, X. Ou, H. Wu, D. Feng, X. H. Chen, Y. Zhang, *Nat. Nanotechnol.* **2014**, *9*, 372.
[11] D. A. Chenet, Oak. Aslan, P. Y. Huang, C. Fan, A. M. van der Zande, T. F. Heinz, J. C. Hone, *Nano Lett.* **2015**, *15*, 5667.
[12] X.-F. Qiao, J.-B. Wu, L. Zhou, J. Qiao, W. Shi, T. Chen, X. Zhang, J. Zhang, W. Ji, P.-H. Tan, *Nanoscale* **2016**, *8*, 8324.
[13] H. Zhao, J. Wu, H. Zhong, Q. Guo, X. Wang, F. Xia, L. Yang, P. Tan, H. Wang, *Nano Res.* **2015**, *8*, 3651.
[14] B. Liu, M. Köpf, A. N. Abbas, X. Wang, Q. Guo, Y. Jia, F. Xia, R. Weihrich, F. Bachhuber, F. Pielnhofer, H. Wang, R. Dhall, S. B. Cronin, M. Ge, X. Fang, T. Nilges, C. Zhou, *Adv. Mater.* **2015**, *27*, 4423.
[15] G. Hu, T. Albrow-Owen, X. Jin, A. Ali, Y. Hu, R. C. T. Howe, K. Shehzad, Z. Yang, X. Zhu, R. I. Woodward, T.-C. Wu, H. Jussila, J.-B. Wu, P. Peng, P.-H. Tan, Z. Sun, E. J. R. Kelleher, M. Zhang, Y. Xu, T. Hasan, *Nat. Commun.* **2017**, *8*, 278.
[16] H. Yuan, X. Liu, F. Afshinmanesh, W. Li, G. Xu, J. Sun, B. Lian, A. G. Curto, G. Ye, Y. Hikita, Z. Shen, S.-C. Zhang, X. Chen, M. Brongersma, H. Y. Hwang, Y. Cui, *Nat. Nanotechnol.* **2015**, *10*, 707.
[17] Q. Guo, A. Pospischil, M. Bhuiyan, H. Jiang, H. Tian, D. Farmer, B. Deng, C. Li, S.-J. Han, H. Wang, Q. Xia, T.-P. Ma, T. Mueller, F. Xia, *Nano Lett.* **2016**, *16*, 4648.
[18] M. Huang, M. Wang, C. Chen, Z. Ma, X. Li, J. Han, Y. Wu, *Adv. Mater.* **2016**, *28*, 3481.
[19] F. Liu, S. Zheng, X. He, A. Chaturvedi, J. He, W. L. Chow, T. R. Mion, X. Wang, J. Zhou, Q. Fu, H. J. Fan, B. K. Tay, L. Song, R.-H. He, C. Kloc, P. M. Ajayan, Z. Liu, *Adv. Funct. Mater.* **2016**, *26*, 1169.
[20] D. Li, H. Jussila, L. Karvonen, G. Ye, H. Lipsanen, X. Chen, Z. Sun, *Sci. Rep.* **2015**, *5*, 15899.
[21] F. Yang, X. Wang, D. Zhang, J. Yang, D. Luo, Z. Xu, J. Wei, J.-Q. Wang, Z. Xu, F. Peng, X. Li, R. Li, Y. Li, M. Li, X. Bai, F. Ding, Y. Li, *Nature* **2014**, *510*, 522.
[22] W. Kaminsky, K. Claborn, B. Kahr, *Chem. Soc. Rev.* **2004**, *33*, 514.
[23] H. B. Ribeiro, M. A. Pimenta, C. J. S. de Matos, R. L. Moreira, A. S. Rodin, J. D. Zapata, E. A. T. de Souza, A. H. Castro Neto, *ACS Nano* **2015**, *9*, 4270.
[24] M. Long, A. Gao, P. Wang, H. Xia, C. Ott, C. Pan, Y. Fu, E. Liu, X. Chen, W. Lu, T. Nilges, J. Xu, X. Wang, W. Hu, F. Miao, *Sci. Adv.* **2017**, *3*, e1700589.
[25] X. Wang, Y. Li, L. Huang, X.-W. Jiang, L. Jiang, H. Dong, Z. Wei, J. Li, W. Hu, *J. Am. Chem. Soc.* **2017**, *139*, 14976.
[26] S. Yang, C. Hu, M. Wu, W. Shen, S. Tongay, K. Wu, B. Wei, Z. Sun, C. Jiang, L. Huang, Z. Wang, *ACS Nano* **2018**, *12*, 8798.
[27] D.-J. Xue, J. Tan, J.-S. Hu, W. Hu, Y.-G. Guo, L.-J. Wan, *Adv. Mater.* **2012**, *24*, 4528.
[28] Z. Tian, C. Guo, M. Zhao, R. Li, J. Xue, *ACS Nano* **2017**, *11*, 2219.
[29] L.-D. Zhao, G. Tan, S. Hao, J. He, Y. Pei, H. Chi, H. Wang, S. Gong, H. Xu, V. P. Dravid, C. Uher, G. J. Snyder, C. Wolverton, M. G. Kanatzidis, *Science* **2016**, *351*, 141.
[30] Z. Zhou, M. Long, L. Pan, X. Wang, M. Zhong, M. Blei, J. Wang, J. Fang, S. Tongay, W. Hu, J. Li, Z. Wei, *ACS Nano* **2018**, *12*, 12416.
[31] T. A. Searles, Y. Imanaka, T. Takamasu, H. Ajiki, J. A. Fagan, E. K. Hobbie, J. Kono, *Phys. Rev. Lett.* **2010**, *105*, 017403.
[32] Y.-Y. Sun, M. L. Agiorgousis, P. Zhang, S. Zhang, *Nano Lett.* **2015**, *15*, 581.
[33] S. Niu, H. Huyan, Y. Liu, M. Yeung, K. Ye, L. Blankemeier, T. Orvis, D. Sarkar, D. J. Singh, R. Kapadia, J. Ravichandran, *Adv. Mater.* **2017**, *29*, 1604733.

[34] S. Niu, G. Joe, H. Zhao, Y. Zhou, T. Orvis, H. Huyan, J. Salman, K. Mahalingam, B. Urwin, J. Wu, Y. Liu, T. Tiwald, S. B. Cronin, B. Howe, M. Mecklenburg, R. Haiges, D. J. Singh, H. Wang, M. A. Kats, J. Ravichandran, *Nat. Photonics* **2018**, *12*, 392.
[35] S. Niu, H. Zhao, Y. Zhou, H. Huyan, B. Zhao, J. Wu, S. B. Cronin, H. Wang, J. Ravichandran, *Chem. Mater.* **2018**, *30*, 4897.
[36] J. L. Musfeldt, D. B. Tanner, A. J. Paine, *J. Opt. Soc. Am. A* **1993**, *10*, 2648.
[37] O. B. Aslan, D. A. Chenet, A. M. van der Zande, J. C. Hone, T. F. Heinz, *ACS Photonics* **2016**, *3*, 96.
[38] R. W. Havener, H. Zhuang, L. Brown, R. G. Hennig, J. Park, *Nano Lett.* **2012**, *12*, 3162.
[39] J.-B. Wu, X. Zhang, M. Ijäs, W.-P. Han, X.-F. Qiao, X.-L. Li, D.-S. Jiang, A. C. Ferrari, P.-H. Tan, *Nat. Commun.* **2014**, *5*, 5309.
[40] J.-B. Wu, Z.-X. Hu, X. Zhang, W.-P. Han, Y. Lu, W. Shi, X.-F. Qiao, M. Ijiäs, S. Milana, W. Ji, A. C. Ferrari, P.-H. Tan, *ACS Nano* **2015**, *9*, 7440.
[41] J.-B. Wu, M.-L. Lin, X. Cong, H.-N. Liu, P.-H. Tan, *Chem. Soc. Rev.* **2018**, *47*, 1822.
[42] X. Ling, S. Huang, E. H. Hasdeo, L. Liang, W. M. Parkin, Y. Tatsumi, A. R. T. Nugraha, A. A. Puretzky, P. M. Das, B. G. Sumpter, D. B. Geohegan, J. Kong, R. Saito, M. Drndic, V. Meunier, M. S. Dresselhaus, *Nano Lett.* **2016**, *16*, 2260.
[43] S. Zhang, N. Zhang, Y. Zhao, T. Cheng, X. Li, R. Feng, H. Xu, Z. Liu, J. Zhang, L. Tong, *Chem. Soc. Rev.* **2018**, *47*, 3217.
[44] J.-B. Wu, H. Zhao, Y. Li, D. Ohlberg, W. Shi, W. Wu, H. Wang, P.-H. Tan, *Adv. Opt. Mater.* **2016**, *4*, 756.
[45] R. Loudon, *Adv. Phys.* **1964**, *13*, 423.
[46] G. Kresse, J. Furthmüller, *Phys. Rev. B* **1996**, *54*, 11169.
[47] P. E. Blöchl, *Phys. Rev. B* **1994**, *50*, 17953.
[48] G. Kresse, D. Joubert, *Phys. Rev. B* **1999**, *59*, 1758.
[49] F. Tran, P. Blaha, *Phys. Rev. Lett.* **2009**, *102*, 226401.
[50] S. Baroni, S. de Gironcoli, A. Dal Corso, P. Giannozzi, *Rev. Mod. Phys.* **2001**, *73*, 515.